VARIABILITY OF PRIMARY AND SCATTER SIGNAL IN DECT:

AN EXPLORATORY STUDY

Daniel Arroyo-Portilla[1], Jeffrey F. Williamson[2], Bruce Whiting[3], Joseph A. O'Sullivan[4], Mariela A. Porras-Chaverri[5].

[1]Escuela de Física, Universidad de Costa Rica.
[2]Deparment of Radiation Oncology, Washington University School of Medicine, St. Louis, MO 63110
[3]Radiology Department, University of Pittsburgh, Pittsburgh PA
[4]Department of Electrical and Systems Engineering, Washington University, St. Louis, MO
[5]Centro de Investigación en Ciencias Atómicas, Nucleares y Moleculares, Universidad de Costa Rica

Abstract

The intensity and distribution of the primary and scatter radiation that reaches the detectors in a Computed Tomography (CT) scanner has a direct impact in the clinical usability of the image reconstructed. The amount of radiation that reaches each detector depends on both the geometrical and material characteristics of the CT scanner, as well as the image acquisition parameters and patient characteristics. The purpose of this work is to determine the range of variation of total signal that reaches CT detectors in a computational simulation of a commercial CT scanner, using radiation transport Monte Carlo methods, as a study of the characteristics of a particular scanner configuration. The geometry was based on that of a commercially available CT scanner. The gadolinium oxysulfide detectors are separated by highly attenuating septa. In this exploratory study, two sets of monoenergetic beams were used, 45 keV and 80 keV. Scatter signal of the phantom is determined and the amount of primary signal that arrives to the detector is not evenly distributed on the module.

Resumen

La cantidad y distribución de radiación primaria y secundaria depositada en los detectores de un escáner de tomografía computarizada (TC), tienen un impacto directo en la reconstrucción de imágenes clínicas. La cantidad de radiación en cada detector depende de la geometría y los materiales característicos del escáner TC, además de los parámetros de adquisición y las características del paciente. El propósito de este trabajo es determinar el rango de variación de la señal que llega a los detectores en una simulación computacional de un escáner TC comercial, utilizando métodos Monte Carlo para el transporte de radiación, y un estudio de las características particulares de la configuración del escáner. La geometría es de un escáner TC comercial. Los detectores de oxisulfuro de gadolinio están separados por septa altamente atenuantes. Este estudio exploratorio utilizó dos energías monoenergéticas para el haz, 45 keV y 80 keV. Se determinó la señal de dispersión del maniquí y que la señal primaria que llega a los detectores no se encuentra uniformemente distribuida a través del módulo.

[1]*Corresponding Author: daniel.arroyoportilla@ucr.ac.cr

I.   INTRODUCTION

Computed tomography (CT) images are widely used in many countries around the world. In the United States alone, approximately 74 million scans were performed in 2017 (Schultz, 2020). Dual-energy computed tomography (DECT) scanners combine two different energy sources to acquire images and achieve a better differentiation of materials inside the phantom (Johnson, 2007). DECT imaging is also capable of taking 3D cross-sectional images of the body with enough details to differentiate soft tissues, blood vessel and bones. These images can be used in the identification of many types of cancer and abnormal structures inside the body, thanks to the different attenuation coefficients of matter (Lam, 2015). DECT imaging techniques can be used to quantify two-independent characteristics of the medium occupying each voxel, typically electron density and a surrogate for atomic composition. This enables radiological quantities, e.g., linear attenuation coefficients and charged-particle stopping powers to be more accurately mapped.

In CT, photon transmission profiles are measured via a detector array opposing a fanshaped x-ray beam that orbits around the body. In each angular projection, the beam is attenuated by the body structures allowing the differentiation of materials due to their different attenuation coefficients. The attenuated signal reaches the sensitive detector volumes (referred as detector elements in this work). These elements generate an electrical signal that is collected and processed by a computer for further reconstruction of the image.

The signal received in the elements has two main components: that due to primary radiation and scatter radiation. The primary signal arises from photons emitted by the source that deposits its energy into the elements without interacting with other structures. This signal is used in the image reconstruction process to generate the image. On the other hand, the scatter radiation signal, adversely affects the image quality. This signal arises from photons that interact with the patient's body before reaching the detector array.

Reduction of the scatter radiation that reaches the detector elements is achieved using antiscatter grids (ASG). These are structures that block scattered photons that deviate from the source-detector element trajectory. However, not all the scatter radiation will be blocked. In particular, the forward-directed scatter coherent scattering and the scatter produced in scanner structures close to the source (such as the bowtie filter) are able to reach the detector elements. The elements cannot differentiate primary from scatter radiation, causing that some of the scatter signal behaves as a primary event coming directly from the source.

The purpose of this work is to present a preliminary implementation of a Monte Carlo simulation of a typical CT scanner. It is important to say that the actual objective of this preliminary report is to confirm that the scanner geometry assumed and the physical plausibility of the results. The work participated on the LANSPA 2020 as a student presentation. In future work in our research group, we will use this application to determine the scatter radiation for a wider range of energies and image acquisitions geometries.

II.   MATERIALS AND METHODS

The simulations were performed using the Geant4 toolkit (version 10.06.p03) for the C++ programming language. This software simulates the trajectory of particles through matter and their interactions using Monte Carlo methods. (Agostinelli, 2003). The Geant4 Physics List used for these simulations was *G4EmStandardPhysics*.

The simulations developed in this work are based on the B3b Geant4 example code, which was originally created by Michael Maire to simulate a Positron Emitted Tomography system. This user code can be found in basic examples provided by Geant4. (Geant4, n.d.). The original geometry of this C++ example application is modified so it can easily add any number of modules per detector and elements per module, change the distribution angle of modules in the detector array and even add more than one detector like slices to the system. Simplifying the task of modeling the geometry of the CT scanner of interest.

The modified B3b application allows for a flexible geometry, in which the number of detector modules and detector elements can be easily changed to model a particular scanner geometry. In the present work, we use only a geometry based on a CT scanner available to our group. All scanner geometry details were obtained directly from the manufacturer and remain proprietary information (Evans, 2013), (Liu, 2021).

The transverse-plane geometry through the center of the detector array used in this study is presented in Figure 1. This figure shows a slice of the system where head-size phantom is centered on the scanner isocenter with a 30 cm diameter field of view (FOV) with axial data acquisition. The axial collimation of the fan beam was 12.00 mm. (Miyata, 2020). The detector array is located at the bottom of the figure. There are 51 linear detector-array modules placed on an arc each consisting of 16 rows of 16 detector elements. The distance from the proximal central septum of each module to the source was and the 1155.70 mm. Figure 2 shows a detail of the detector module. All results were normalized by 1×10^9 the number of photons exiting the source.

Figure 1. Sketch of the geometry used in the simulation, distance from source to phantom and detector is shown and aperture of the FOV.

Figure 2. Sketch of the module dimensions and materials, dimensions of the different structures are shown. The scale has been greatly exaggerated.

The geometry consists of three main components:

1. X-ray source: two monoenergetic sources with energies of 45 keV and 80 keV, emitted towards the FOV. These energies were selected as a simplified representation for the energies of a DECT x-ray spectrum. (Forghani, 2017). No bowtie filter or other scanner structures were included in this first approximation to the geometry. See Figure 1.
2. Patient phantom: a 21.0 cm diameter water cylinder, with a thickness of 14 mm. (Nickoloff, 2003). The diameter of the phantom approximates the head of an adult patient and is typical of CT phantoms. The phantom is fully contained within the FOV. See Figure 1.
3. Detector array: the array contains 51 modules positioned located on a circular arc as shown in Figure 1. Each module contains 16 elements, seen in Figure 2, made of gadolinium oxysulfide, a ceramic scintillator material commonly used in these scanners (Shefer, 2013). Each module has a

depth of 1.4 mm along the z-axis see Figure 2. Each one of the elements are separated by molybdenum septa. Molybdenum is well known for its blocking properties on ionizing energies at our energy range of interest (Shefer, 2013), blocking most of the scatter signal.

The septa face towards the x-ray source to allow passage of photons into the detector elements of the beams coming from a narrow solid angle, such as those corresponding to event 1 in Figure 2. This effectively prevents scatter photons (such as those from event 2a) from reaching the detector elements. However, even with the presence of septa, there is still scatter radiation that reaches the detector elements, as is the case with event 2b. Quantification of the scatter radiation that reaches the detectors will allow correction for scatter during the image reconstruction process.

In this work, four different geometries were simulated for two different photon energies from the source, for a total of eight simulations. Each simulation is identified as follows:

S1 – No phantom and no septa, 45 keV source.
S2 – Water phantom and no septa, 45 keV source.
S3 – No phantom and molybdenum septa, 45 keV source.
S4 – Water phantom and molybdenum septa, 45 keV source.
S5 – No phantom and no septa, 80 keV source.
S6 – Water phantom and no septa, 80 keV source.
S7 – No phantom and molybdenum septa, 80 keV source.
S8 – Water phantom and molybdenum septa, 80 keV source.

III. RESULTS AND DISCUSSION

Figure 3 shows the relative intensity of the signal reaching the detector elements for simulations that do not include septa. The values shown in this figure were obtained by normalizing the results from S2 with S1 for the 45 keV source, and S6 normalized by S5 for the 80 keV source. Each of the ticks in the horizontal axis corresponds to one module with sixteen elements.

This an idealized geometry but was included as a means to recognize the effect of the septa in total signal that reaches the detector elements. A maximum of 25.9% signal reduction was found when comparing non-septa simulations with septa simulations. As expected, a drop in total signal due to the phantom presence can be observed. The line corresponding to a 45 keV source shows irregularities below the center of the phantom, due to attenuation of the signal and increased thickness of the phantom at its center. In the case of the 80 keV curve, the curve is smoother due to less attenuation of the signal.

Several modules that are out of the FOV, corresponding to detector modules numbered 1 to 13 and from 39 to 51, are not included in this analysis.
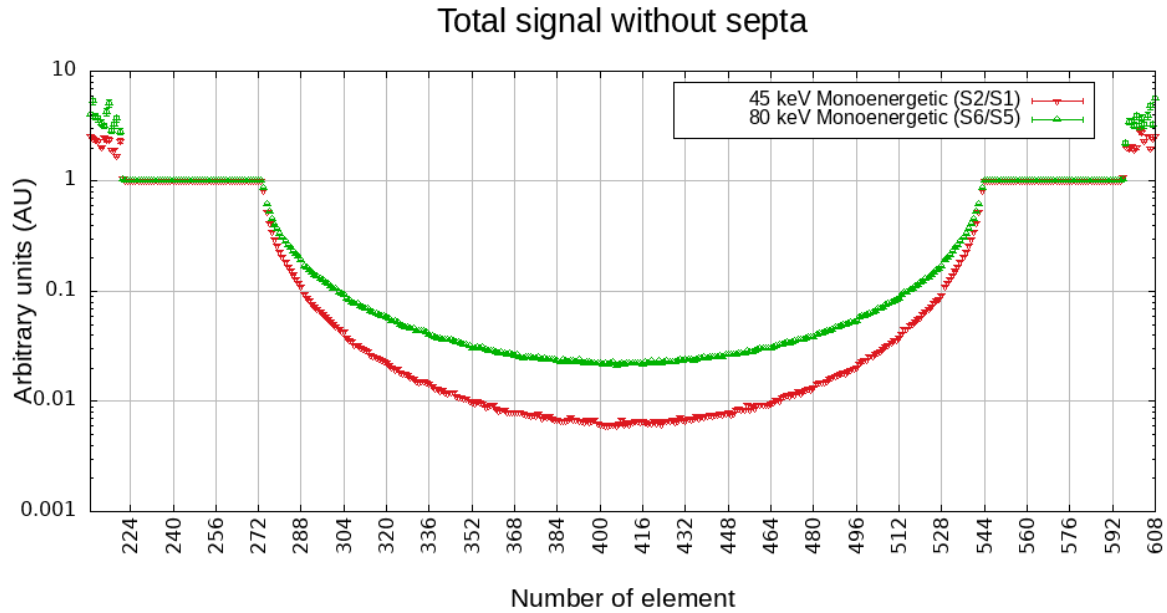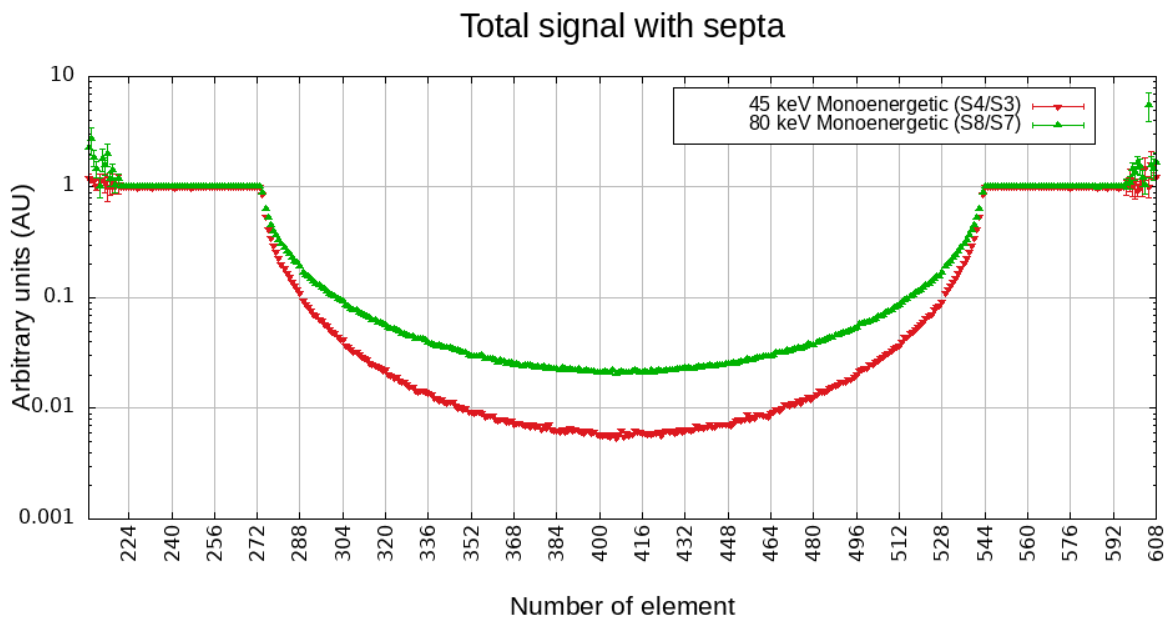
Total signal without septa

Figure 3. Relative intensity on elements of the detector for two set of energies without the septa. The formula used for the 45 keV energy is S2/S1 and for the 80keV is S6/S5.

Figure 4 shows a more realistic scenario, including the septa in the simulation. The data was generated by normalizing S4 by S3 for the 45 keV and S8 by S7 for the 80 keV. It can be observed that the previous considerations for boundaries and influence of the phantom due to the energy used are the same as those from Figure 3. The difference between Figures 3 and 4 resides in the influence of the "full" scatter signal on the elements in Figure 3 compared to the much-reduced scatter signal on Figure 4 due to the ASG.

Total signal with septa

Figure 4. Relative intensity on elements of the detector for two set of energies with the Septa. The formula used for the 45 keV energy is S4/S3 and for the 80keV is S8/S7.
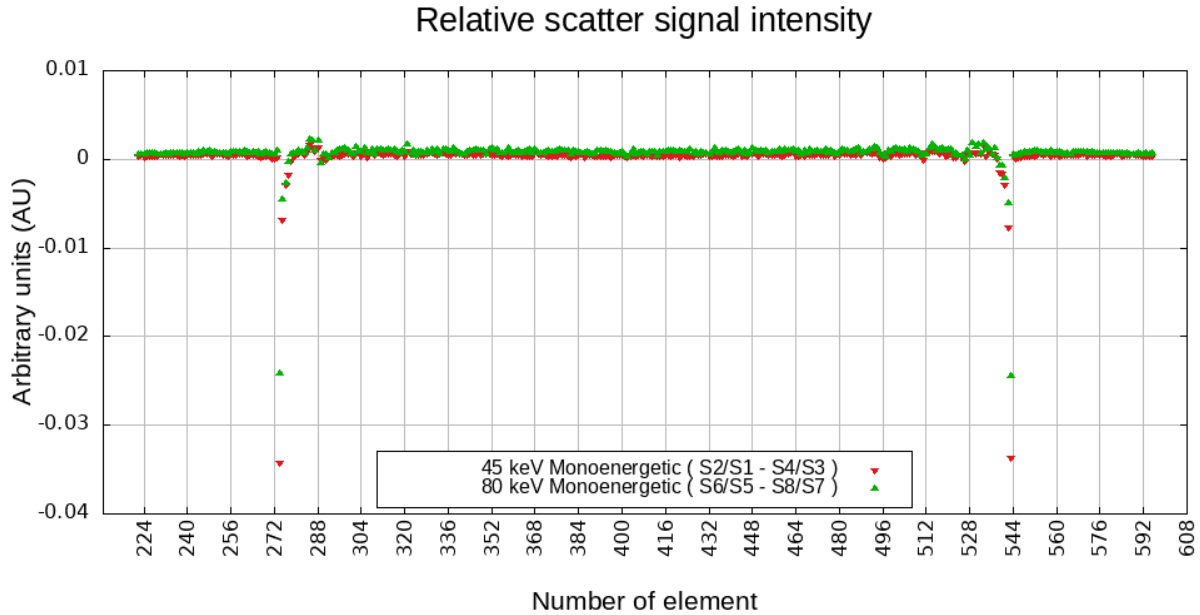
Figure 5. Estimated scatter radiation profile on each element, for two sets of energies, approximated by the difference between uncollimated total signal and total signal collimated by ASG.

Figure 5 shows a comparison of the estimated scatter signal of the phantom. The data was obtained by subtracting the results of S4 normalized by S3 from the results of the S2 normalized by S1 for the 45 keV, and similarly using S8 normalized by S7 and S6 normalized by S5 for the 80 keV. This analysis provides a preliminary approximation to the upper limit of the scatter signal from the phantom (event 2b in Figure 2). This approach is limited as it does not distinguish the sources of the scatter and does not account for any effects of the ASG on the primary signal and further assumes that the ASG reduces the scatter to a negligible level. Although the presence of the phantom can be inferred from its shadow, the profiles are different from the ones showing the total signal. This is to be expected as the scatter signal spreads out from the direction of the primary beam and the scatter signal from 45 keV shows more spread than the signal from 80 keV.

Based on the results of this preliminary study, it can be concluded that the Geant4 simulation developed as part of this work can be used to simulate CT scanner geometries. In further studies, our group will utilize this framework to quantify the impact and sources of scatter in the total signal that reaches the detectors, and validate these results via experiments, as well as compare to other Geant4 applications developed by our collaborators (Liu, 2021).

IV.   REFERENCES

Agostinelli, S., Allison, J., Amako, K., Apostolakis, J., Araujo, H., Arce, P., Asai, M., Axen, D., Banerjee, S., Barrand, G., Behner, F., Bellagamba, L., Boudreau, J., Broglia, L., Brunengo, A., Burkhardt, H., Chauvie, S., Chuma, J., Chytracek, R., … Zschiesche, D. (2003). GEANT4 - A simulation toolkit. *Nuclear Instruments and Methods in Physics Research, Section A: Accelerators, Spectrometers, Detectors and Associated Equipment*, *506*(3), 250–303. https://doi.org/10.1016/S0168-9002(03)01368-8

Evans, J. D., Whiting, B. R., Politte, D. G., O'Sullivan, J. A., Klahr, P. F., & Williamson, J. F. (2013). Experimental implementation of a polyenergetic statistical reconstruction algorithm for a commercial fan-beam CT scanner. *Physica Medica*, *29*(5), 500–512. https://doi.org/10.1016/j.ejmp.2012.12.005

Forghani, R., De Man, B., & Gupta, R. (2017). Dual-Energy Computed Tomography: Physical Principles, Approaches to Scanning, Usage, and Implementation: Part 2. *Neuroimaging Clinics of North America 27*(3), 385–400. W.B. Saunders. https://doi.org/10.1016/j.nic.2017.03.003

Geant4 examples: Example B3. (n.d.). Retrieved November 20, 2020, from http://geant4-userdoc.web.cern.ch/geant4-userdoc/Doxygen/examples_doc/html/ExampleB3.html

Johnson, T. R. C., Krauß, B., Sedlmair, M., Grasruck, M., Bruder, H., Morhard, D., Fink, C., Weckbach, S., Lenhard, M., Schmidt, B., Flohr, T., Reiser, M. F., & Becker, C. R. (2007). Material differentiation by dual energy CT: Initial experience. *European Radiology*, *17*(6), 1510–1517. https://doi.org/10.1007/s00330-006-0517-6

Lam, S., Gupta, R., Kelly, H., Curtin, H. D., & Forghani, R. (2015). Multiparametric Evaluation of Head and Neck Squamous Cell Carcinoma Using a Single-Source Dual-Energy CT with Fast kVp Switching: State of the Art. *Cancers*, *7*(4), 2201–2216. https://doi.org/10.3390/cancers7040886

Liu, R., Zhang, S., Zhao, T., O'Sullivan, J. A., Williamson, J. F., Webb, T., Porras-Chaverri, M., & Whiting, B. (2021). Impact of bowtie filter and detector collimation on multislice CT scatter profiles: A simulation study. *Medical Physics*, 48(2), 852–870. https://doi.org/10.1002/mp.14652

Miyata, T., Yanagawa, M., Hata, A., Honda, O., Yoshida, Y., Kikuchi, N., Tsubamoto, M., Tsukagoshi, S., Uranishi, A., & Tomiyama, N. (2020). Influence of field of view size on image quality: ultra-high-resolution CT vs. conventional high-resolution CT. *European Radiology*, *30*(6), 3324–3333. https://doi.org/10.1007/s00330-020-06704-0

Nickoloff, E. L., Dutta, A. K., & Lu, Z. F. (2003). Influence of phantom diameter, kVp and scan mode upon computed tomography dose index. *Medical Physics*, *30*(3), 395–402. https://doi.org/10.1118/1.1543149

Schultz, C. H., Fairley, R., Murphy, L. S. L., & Doss, M. (2020). The Risk of Cancer from CT Scans and Other Sources of Low-Dose Radiation: A Critical Appraisal of Methodologic Quality. *Prehospital and Disaster Medicine*, *35*(1), 3–16. https://doi.org/10.1017/S1049023X1900520X

Willemink, M. J., & Noël, P. B. (2019). The evolution of image reconstruction for CT—from filtered back projection to artificial intelligence. *European Radiology*, *29*(5), 2185–2195. https://doi.org/10.1007/s00330-018-5810-7

ACKNOWLEDGMENTS